

This document is the accepted manuscript version of the following article:
Niemelä, J. P., Philip, A., Rohbeck, N., Karppinen, M., Michler, J., & Utke, I.
(2021). Mechanics of nanoscale ϵ -Fe₂O₃/organic superlattices toward flexible thin-film magnets. ACS Applied Nano Materials, 4(2), 1692–1701.
<https://doi.org/10.1021/acsanm.0c03163>

Mechanics of Nanoscale ϵ -Fe₂O₃/Organic

Superlattices Towards Flexible Thin-Film Magnets

Janne-Petteri Niemelä,^{1*} Anish Philip,² Nadia Rohbeck,¹ Maarit Karppinen,² Johann Michler,¹
Ivo Utke,¹

¹Laboratory for Mechanics of Materials and Nanostructures, Empa – Swiss Federal Laboratories for Materials Science and Technology, Feuerwerkerstrasse 39, Thun CH-3602, Switzerland.

²Department of Chemistry and Materials Science, Aalto University, FI-00076 Espoo, Finland

*Corresponding author (E-mail: janne-petteri.niemelae@empa.ch)

KEYWORDS: tensile testing, nanoindentation, thin-film fragmentation, flexible magnet, atomic layer deposition, molecular layer deposition, ϵ -Fe₂O₃-organic superlattice, thin film

ABSTRACT:

The state-of-the-art atomic layer deposition (ALD) thin-film technology which is well-integrated with microelectronics and beyond is currently strongly extending towards hybrid materials where organic fragments are inserted within the inorganic matrix through so-called molecular layer deposition (MLD) cycles. This allows the fabrication of nanoscale inorganic-organic superlattices and multilayers directly from the gas phase. These materials are particularly promising for enhancing the mechanical flexibility of the rigid inorganics. Here we demonstrate for ALD/MLD-grown ϵ -Fe₂O₃/Fe-terephthalate superlattice structures that nanoscale (1 ~ 10 nm) Fe-terephthalate interlayers significantly improve the flexibility of ϵ -Fe₂O₃ thin films without sacrificing their

unique high-coercive-field magnetic characteristics. Nanoindentation evaluation indicates that the elastic modulus can be reduced by a factor of two down to 70 ± 20 GPa, while in-situ tensile fragmentation testing demonstrates that the crack onset strain and critical bending radius can be tuned by a factor of three. Modeling of the tensile fragmentation patterns through Weibull statistics shows that cohesive and interfacial shear strain, following the trend for crack onset strain, increase with increasing organic content, while gains for the respective strengths are limited by the simultaneous reduction in elastic modulus. The Fe-terephthalate film exhibits high interfacial shear strain/strength and low tendency for buckling, which highlights its potential to act as an adhesion layer for the ferrimagnetic ϵ -Fe₂O₃ layers. The results are particularly interesting for magnetic recording applications in sustainable next-generation flexible electronics.

1. Introduction

The trend in today's consumer electronics is towards thin and flexible devices. Since magnets are key components in electronics, there is a significant demand for flexible nanoscale magnets, e.g. in magnetic recording devices.¹ Conventional inorganic magnets are brittle and rigid, which poses critical issues in their use in flexible electronics. Organic materials would be superior in flexibility in general, but the organic/molecular magnets so far developed lag far behind their inorganic counterparts regarding the magnetic characteristics, in particular the magnetic transition temperature as well as the magnetization and coercivity.²⁻⁴ Our approach here is to combine the best parts of the two worlds, that is, the superior magnetic characteristics of the inorganic materials and the flexibility of organic materials, by depositing inorganic-organic superlattice thin films using the industrially feasible gas-phase atomic/molecular layer deposition (ALD/MLD) technique.

The little-known ε -Fe₂O₃ phase is an intriguing material for the inorganic magnetic component. It is one of the five iron(III)oxide polymorphs, the other four being the naturally occurring α -Fe₂O₃ (hematite) and γ -Fe₂O₃ (maghemite) phases, the β -Fe₂O₃ phase, and the high-pressure stabilized ζ -Fe₂O₃ (zeta-Fe₂O₃) phase.⁵ Most impressively, the ε -Fe₂O₃ phase is a room-temperature ferrimagnet with an exceptionally high coercive field up to ~ 20 kOe,⁶⁻⁸ a feature that makes it particularly attractive for information storage applications.^{2,9} However, due to its narrow thermal stability window (between maghemite and hematite) in phase-pure form, ε -Fe₂O₃ has thus far been fabricated only in nanoscale, as nanoparticles^{10,11} and thin films.^{6,12} Like other iron oxides, ε -Fe₂O₃ is composed of earth-abundant non-toxic elements, a favorable feature for sustainable technologies.

The atomic layer deposition (ALD) thin-film technique employed here has cemented its position as a driver for (Si-based rigid) microelectronics through enabling conformal coating of high-aspect ratio nanostructures with nanoscale inorganic thin films.^{13,14} It relies on cyclic and self-limiting gas-surface chemical reactions between the sequentially dosed precursor molecules on the growth surface. The cyclic nature of the deposition process ensures unprecedented atomic-level control over the film thickness, while the self-limited nature of the surface reactions guarantees the high level of conformality of the coatings.¹⁵ The latter feature is highly useful as it allows considerably enhanced mass deposition rate, and the direct integration of the coatings on mechanically flexible 3D porous substrates, such as textiles for wearable applications.

The unique features of the parent ALD technology for inorganic materials also apply to the recently strongly emerging combination of ALD and MLD (molecular layer deposition) applied for the growth of hybrid inorganic-organic thin films in nanoscale.¹⁶⁻¹⁹ These materials are typically grown from metal precursors such as trimethylaluminum (TMA),¹⁷ diethylzinc (DEZ),²⁰ and titanium tetrachloride (TiCl₄)²¹ while the organic components are often deposited from aliphatic alcohols

(e.g. ethylene glycol; EG),¹⁷ aromatic alcohols (e.g. hydroquinone; HQ)²¹ or carboxylic acids (e.g. terephthalic acid; TPA)²². Importantly, the combined ALD/MLD technique has already been employed for the fabrication of inorganic-organic superlattices with a range of electrical and thermal transport,²¹ optical,²³ and structural properties.^{24, 25} The elegance in this approach lies in the sub-nanometer level of control of the individual layer thicknesses, as the ALD and MLD cycles can be applied to any pre-designed layer sequence pattern, and in the fact that the entire deposition process can be carried out in a single deposition chamber. These are drastic advances in comparison to multi-chamber approaches, requiring a number of cyclic substrate transfers e.g. between CVD and spin coating setups, recently explored for tailoring mechanical flexibility of inorganic-organic multilayers.²⁶ So far encouraging results on mechanical property tuning have been achieved for ALD/MLD alloys where single-to-few ALD and MLD cycles have been mixed for amorphous metal-organic hybrid films.^{20, 27, 28} In contrast, in this work we focus on the mechanical properties of superlattice thin films with reasonably thick (yet nanoscale) inorganic layers required for unlocking magnetic and other functional material properties.

We recently succeeded in preparing high-quality phase-pure ϵ -Fe₂O₃ thin films through an ALD route from FeCl₃ and H₂O precursors in the temperature range 280–300 °C.²⁹ The films were found to be stable in ambient air, and most remarkably, they could be combined with monomolecular organic interlayers (inserted through MLD cycles of the FeCl₃ and TPA precursors) without destroying the ϵ -Fe₂O₃ structure,^{22, 23} and compromising the high coercive field magnetic property of the ϵ -Fe₂O₃ layers, while simultaneously enhancing the mechanical flexibility of the films.³⁰ In our previous work,³⁰ we provided comprehensive magnetic characterization results and a brief mechanical assessment (critical strain for fracture) for these films. In the present work we now present a detailed account of the mechanical characteristics of these flexible ϵ -Fe₂O₃-based

nanoscale thin film magnets through nanoindentation and tensile testing coupled with in-situ optical microscopy. The tensile fragmentation patterns are modeled through Weibull statistics for information on cohesive and interfacial properties. We show that tailoring the ϵ -Fe₂O₃ thin films through insertion of mechanically dissimilar Fe-terephthalate (Fe-TP) interlayers of nanometric thickness and formation of superlattice structures enables improving the elastic modulus, crack onset strain, critical bending radius, cohesive and interfacial shear strain by factor of two to five. These facts are crucially important for the application of the materials in next-generation flexible devices.

2. Experimental

Four types of thin films were deposited through cyclic ALD/MLD dosing of FeCl₃ (Merck 95 %) as the Fe precursor and either H₂O or TPA (Tokyo Chemical Industry CO. Ltd. > 99.0 %) as the counter reactant. Thin films of ϵ -Fe₂O₃ films were grown from FeCl₃ and H₂O precursors by ALD, and Fe-TP hybrid inorganic-organic films were prepared through the FeCl₃/TPA MLD process. These two processes were then combined through a supercycle approach (in the same deposition chamber) to prepare two types of ALD/MLD superlattice films, labeled as SL1 and SL10 (see also Scheme 1). In both cases, one supercycle consisted of 242 ϵ -Fe₂O₃ cycles and either one (SL1) or ten (SL10) Fe-TP cycles. These supercycles (always starting with ϵ -Fe₂O₃) were repeated 20 times, after which the deposition was finished with 242 ϵ -Fe₂O₃ cycles. The deposition parameters are listed in detail in Table 1, together with the corresponding total film thickness values. The depositions were carried out in a commercial flow-type hot-wall ALD reactor (F-120 by ASM Ltd) at 280 °C on Si (2.0×2.0 cm²) and polyimide (Kapton 200HN) substrates (4.5×4.5 cm² with precut stripes) simultaneously in the same deposition run. Prior to the deposition, the Si substrates were cleaned with ethanol–water mixture and acetone, while the polyimide substrates were cleaned with

isopropyl alcohol and distilled water. The wet cleaning was followed by blow drying, and prior to the film deposition a one-hour wait time at 280 °C was applied to outgas the residual water from the polyimide substrates.

The presence of the terephthalate moieties in the SL films was confirmed using Fourier transform infrared (FTIR, Bruker alpha II) spectroscopy analysis; the spectrum of the Si substrate was subtracted from the spectra of the samples. The targeted ϵ -Fe₂O₃ crystal structure was confirmed by grazing incidence X-ray diffraction (GIXRD; PANalytical X'Pert PRO MPD Alfa 1; Cu K α_1 radiation) measurements. The SL structures were verified from X-ray reflectivity (XRR; PANalytical X'Pert PRO Alfa 1) patterns and through scanning electron microscopy (SEM; Hitachi S4800, 1kV) images of focused-ion-beam cross-sections (Lyra FIB-SEM; cutting 10 nA and polishing 1 nA and 60 pA, voltage was 30 kV). The film thicknesses on polyimide substrates were extracted from the cross-section SEM images (Table 1).

The elastic modulus and hardness of the films were determined by nanoindentation for the films deposited on Si substrates. All experiments were done using a Hysitron Ubi Nanoindenter equipped with a diamond Berkovich tip. The tip area function had been determined before the start of the measurements using a standard piece of fused silica. In order to keep the maximum penetration depth within a tenth of the film thickness (to avoid substrate effects) a few trial indents were performed to determine the correct load for each film. All indents were then run in load control with loading and unloading done over 5 s. The maximum load was held for 2 s. For each film 100 individual indentations were performed. The elastic modulus and hardness values were determined by applying the Oliver and Pharr approach with the Poisson ratio of 0.3 for all the films.

The thin films deposited on the polyimide substrates were characterized through uniaxial tensile strain experiments. They were carried out using a tensile stage (MTI 8000-0010) equipped with a

digital optical microscope (Keyence 500F) for in-situ monitoring of the fragmentation process. The tensile stage was operated at a constant strain rate of $1.4 \times 10^{-4} \text{ s}^{-1}$ by means of displacement control, and microscope images were recorded at strain intervals of 1.4×10^{-4} (i.e. 1 per second) for the subsequent analysis. The strain values were determined via digital image correlation by tracking the distance between pairs of points (polyimide features) on the sample surface. The gauge sections of the samples were $5 \text{ mm} \times 17 \text{ mm}$. The mechanical data in the text represents values normalized to 450 nm film thickness (h_f) via the known $h_f^{-1/2}$ dependence for the crack onset strain (COS) and the saturation crack density.³¹

Magnetic properties of the strained samples were studied using a vibrating sample magnetometer (VSM; Quantum Design PPMS). For the measurements, the samples were first strained, and then a $3 \times 4 \text{ mm}^2$ was cut and glued with GE varnish on a quartz sample holder and set parallel to the applied magnetic field. Magnetization versus magnetic field (M–H) curves were collected by sweeping the magnetic field from -40 to 40 kOe .

Scheme 1. A schematic illustration of the ALD/MLD process for fabrication $\epsilon\text{-Fe}_2\text{O}_3/\text{Fe-TP}$ superlattices, and their structure.

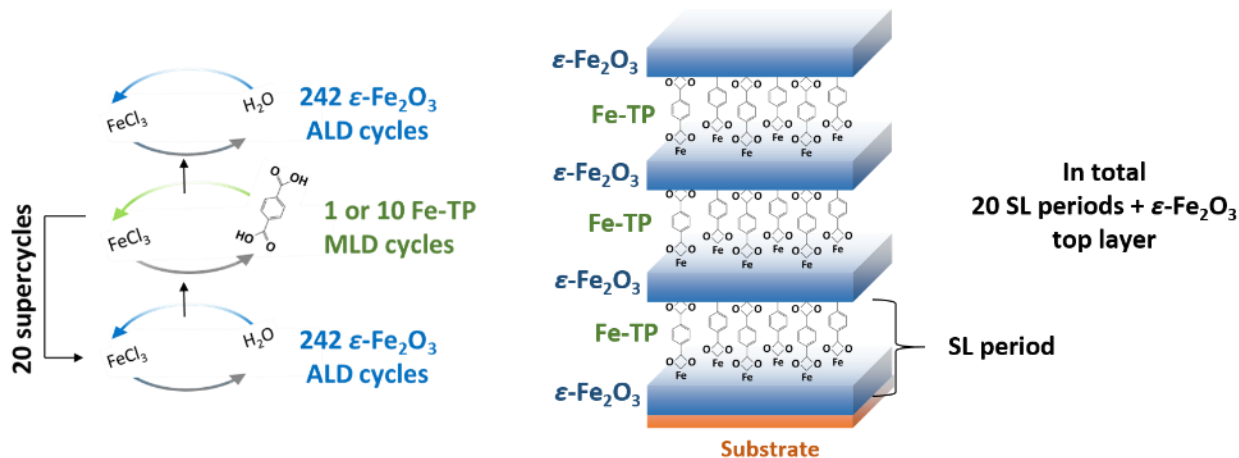


Table 1. The ALD/MLD cycle parameters and film thicknesses. ALD and MLD are conducted through the $\text{FeCl}_3/\text{H}_2\text{O}$ and FeCl_3/TPA processes, respectively. The thickness values were obtained from the SEM cross-section images for the films grown on the polyimide substrates, and the error bar represents the standard deviation over 75-100 measurements.

Sample	ALD cycles	MLD cycles	Supercycles	ALD top cycles	Total cycles	Thickness (nm)
$\epsilon\text{-Fe}_2\text{O}_3$	5081	-	-	-	5081	423 \pm 57
SL1	242	1	20	242	5102	454 \pm 49
SL10	242	10	20	242	5282	663 \pm 64
Fe-TP	-	315	-	-	315	263 \pm 14

3. Results and discussion

3.1 Structural properties

The key structural characteristics are briefly summarized in Figure 1 for selected thin films. The FTIR spectra illustrate that the organic terephthalate moieties are incorporated in the films in the intended manner (Figure 1a). While the spectrum for the iron oxide shows only the phonon modes of the bulk $\epsilon\text{-Fe}_2\text{O}_3$, the spectrum for the SL10 film features, apart from the oxide phonon modes, the carboxylate-group fingerprint with the symmetric (ν_s) and asymmetric (ν_{as}) stretching modes at 1395 and 1505 cm^{-1} , respectively.^{22, 23, 32} The difference in the wavenumber ($\Delta\nu = 110 \text{ cm}^{-1}$) of the ν_s and ν_{as} modes implies bidentate bonding of the terephthalate moiety to the Fe atoms.^{22, 32} The GIXRD spectrum confirms the crystalline nature of the parent oxide film (Figure 1b) with the expected $\epsilon\text{-Fe}_2\text{O}_3$ structure (non-centrosymmetric, orthorhombic, space group $Pna2_1$).^{29, 33, 34} For superlattice films, the diffraction peaks are broader and lower in intensity, and hence the oxide layers have a smaller crystal size and may be partly amorphous in the superlattice films. Importantly, the crystalline domains seem to retain the $\epsilon\text{-Fe}_2\text{O}_3$ structure, as also indirectly judged

from the yet high coercive field values achieved.³⁰ The Fe-TP film crystallizes in a structure that we have not been able to perfectly resolve, although, it has a strong resemblance to the MOF-2 structure typical for Cu-TP and Zn-TP metal organic frameworks.²²

The layer structure of the superlattice films was verified through XRR and cross-section SEM analysis. The XRR pattern for the SL10 shows the SL peaks stemming from constructive interference from the inorganic-organic interfaces (Figure 1c). Due to the high thickness of the film (423 nm by SEM), and its rough surface, the typical interference pattern corresponding to the total thickness of the film is not observed. The cross-sectional SEM image for the SL10 sample

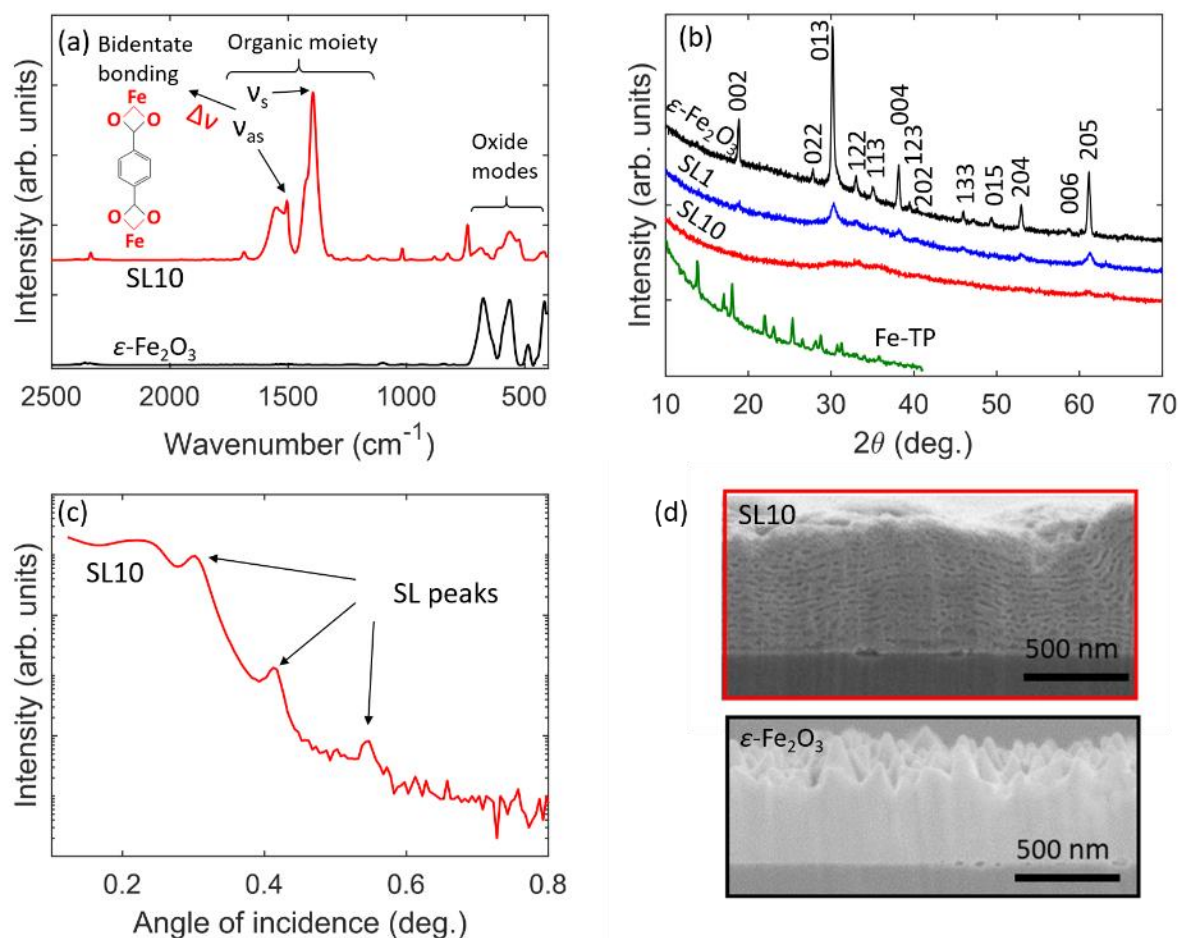


Figure 1. Representative structural characteristics for selected thin films: (a) Fourier transform infrared spectra, (b) x-ray diffraction patterns, (c) an x-ray reflection pattern, and (d) cross-sectional SEM³⁰ images.

illustrates the layer structure,³⁰ in line with the XRR observation (Figure 1d). By comparing the images for the ϵ -Fe₂O₃ and SL10 films, it is observed that the surface morphology of the films transitions from pointy pyramidal roughness for ϵ -Fe₂O₃, to a texture with broader surface features for SL10. Moreover, the film thicknesses extracted from the cross-sectional SEM images were used to calculate the growth-per-cycle (GPC) values for the ALD/MLD processes on polyimide substrate. The values of 0.83 Å/cycle and of 8.3 Å/cycle were obtained for the 423-nm-thick ϵ -Fe₂O₃ and for the 263-nm-thick Fe-TP films, respectively; these values are in a reasonable agreement with the previously reported values of 0.65 Å/cycle and 11 Å/cycle for ~ 100-nm films on Si substrates.²³ Expectedly, the high GPC value for Fe-TP increases the average GPC for the SL1 (0.89 Å/cycle) and for the SL10 (1.26 Å/cycle) above that for the ϵ -Fe₂O₃ film. More details on the structural characteristics of our ϵ -Fe₂O₃, Fe-TP and ϵ -Fe₂O₃/Fe-TP superlattice films can be found in our previous works.^{22, 23, 29, 30}

3.2 Nanoindentation

Despite their crucial importance for sustainable flexible electronics, mechanical properties of (magnetic) iron oxides have been very little explored. Here we first present nanoindentation results for the ϵ -Fe₂O₃ phase, and then the tailoring of its elastic modulus and hardness through the insertion of the Fe-TP interlayers. A series of load-controlled indents were performed, such that the maximum penetration depth of the indenter tip was between 20 and 40 nm. Figure 2a shows the averaged load vs. displacement graphs from these experiments. It can be seen that the load required to reach the same penetration depth progressively decreases throughout the material series from ϵ -Fe₂O₃ to Fe-TP, that is the materials become softer with the increasing organic content. A

distinctive feature for the hybrid Fe-TP material is that upon indentation it immediately exhibits plasticity (similar to Al-based MLD hybrid materials).^{35, 36}

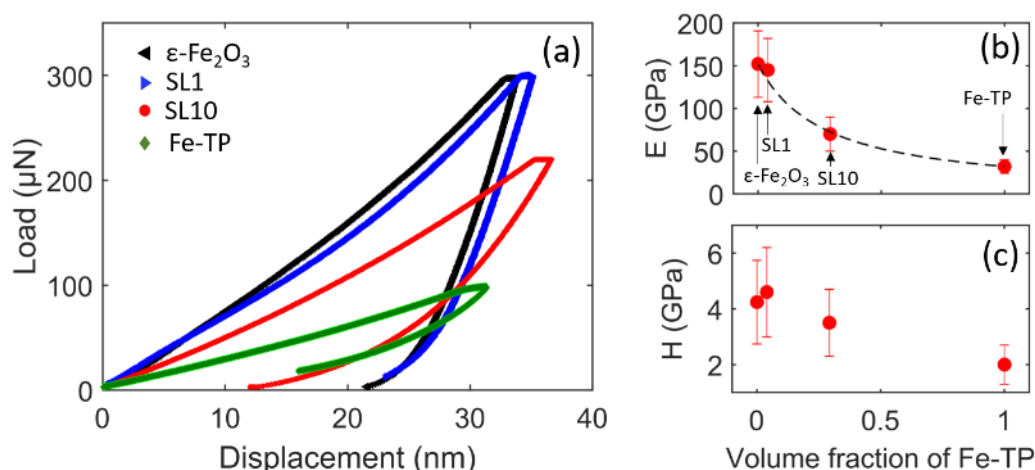


Figure 2. (a) Representative load-displacement graphs from the nanoindentation experiments. (b) Elastic modulus (E), and (c) Hardness (H) values extracted from the load-displacement curves as a function of the Fe-TP/(Fe-TP + ϵ -Fe₂O₃) volume fraction. The volume fractions are based on thickness values for the individual layers in the superlattice, estimated from the GPC values for the single-layer films (0.83 Å/cycle for ϵ -Fe₂O₃ and 8.3 Å/cycle for Fe-TP). In (b) the dashed line represents the rule-of-mixtures prediction for a multilayer material (Reuss formula), respectively.

Elastic modulus and hardness values were extracted from the unloading slope of the load-displacement curve as 152 ± 39 GPa and 4.2 ± 1.5 GPa for the parent ϵ -Fe₂O₃ phase. The modulus value is similar to values for other oxide thin films by the ALD technique, e.g. 160-200 GPa for Al₂O₃ and around 150 GPa for ZnO films,^{20, 28, 37} and somewhat lower than 235 GPa for α -Fe₂O₃ thin films by filtered arc deposition.³⁸ On the other hand the hardness value is somewhat lower than the 9-13 GPa for ALD Al₂O₃, 8-13 GPa for ALD ZnO,^{20, 28, 37} and 17 GPa for the α -Fe₂O₃ thin films by filtered arc deposition.³⁸ The elastic modulus and hardness for the hybrid Fe-TP thin film are 32 ± 8 GPa and 2.0 ± 0.7 GPa, respectively, substantially lower than for our ϵ -Fe₂O₃ film. The modulus value is comparable to the values in the range of 20-40 GPa reported for the similar Al-based (TMA/EG process)^{28, 39, 40} and Zn-based (DEZ/HQ process)²⁰ hybrid materials with

short/rigid organic units. The value falls in the regime typical for composite materials,⁴¹ being yet clearly higher than the polymeric 4.6 GPa for Al-based MLD hybrid films with flexible long-chain organic units (TMA/decanediol process).³⁶ The similarity of the modulus value for the crystalline Fe-TP film with bidentate metal-oxygen-carbon bonding (see also Figure 1a) to the values for amorphous Al-based (TMA/EG process) and Zn-based hybrids (DEZ/HQ process) with monodentate metal-oxygen-carbon bonding indicates that crystallinity or the bonding scheme do not dramatically affect the modulus values. The hardness value for our Fe-TP film is about two times higher than the values around 1 GPa for the amorphous Al-based (TMA/EG process) and Zn-based (DEZ/HQ process) hybrid materials; a plausible explanation for this difference is the crystalline nature of our Fe-TP hybrid material.^{37, 42}

The notably dissimilar mechanical characteristics for the ϵ -Fe₂O₃ and Fe-TP films open the possibility for tailoring the mechanical properties of the ϵ -Fe₂O₃ through insertion of Fe-TP interlayers and formation of superlattice structures through the combinatorial ALD/MLD route. The superlattice thin film in which each organic layer is deposited through one MLD cycle (SL1) shows indentation characteristics that are virtually identical to those for the ϵ -Fe₂O₃ film (Figure 2), that is, monomolecular organic interlayers are not sufficiently thick to substantially contribute their mechanical character to the superlattice. This is understandable, as (as estimated from single-layer growth-per-cycle values) the volume fraction corresponding to the Fe-TP layers is only 0.04 in case of SL1 (Figure 2 b and c). For SL10 the increase in the thickness of the Fe-TP interlayers increases the volume fraction of Fe-TP to 0.29, and consequently the modulus and hardness values decrease down to 70 ± 20 and 3.5 ± 1.2 GPa, respectively. The modulus values can be compared to the rule-of-mixtures prediction for two-component multilayer materials through the Reuss formula $1/E_R = f_1/E_1 + f_2/E_2$ (cross-plane stress).⁴³ Here f represents volume fraction, E is elastic modulus,

and the indices 1 and 2 refer to the values for the ε -Fe₂O₃ and Fe-TP single-layer thin films (Figure 2 b). It can be seen that for the SL10 film the elastic modulus value is well predicted by the Reuss formula, that is, the decrease in the modulus value can be explained by the lamination effect of the two dissimilar materials. It is also evident through the rule of mixtures that organic interlayers enable much broader tuning range for the elastic modulus of superlattice/multilayer materials that what could be achievable by insertion of dissimilar oxide interlayers.

3.3 Fragmentation properties

Mechanical fragmentation properties of the films were studied via uniaxial tensile strain testing coupled with in-situ optical microscopy for the films deposited on the polyimide substrates. The samples were strained at a constant strain rate without any visual changes in the film morphology until the observation of the first crack, perpendicular to the straining axis, at the crack onset strain (COS). Micrographs of the film surface at the crack onset strain, and under various following strain states, are shown in Figure 3 for the ε -Fe₂O₃ film and SL10 film as an example. Crack onset strain provides us with a direct metric of stretchability of the film material, while flexibility of the film-substrate system can be described in terms of critical bending radius $R_c = (h_s + h_f)/(2\text{COS})$, where h_f and h_s are the thicknesses of the film and the substrate, respectively. The COS value of the films increases from 0.33 % for ε -Fe₂O₃ to 1.07 % for the SL10 sample (Table 2), as a sign of substantial increase of stretchability with increasing organic content in the films (the relative increase is as high as 220 %). The increasing trend for stretchability directly translates into an increasing trend for flexibility: the R_c value decreases from 7.7 ± 0.3 for our ε -Fe₂O₃ films to 2.4 ± 0.3 mm for the SL10 film (on 50- μ m polyimide substrate).

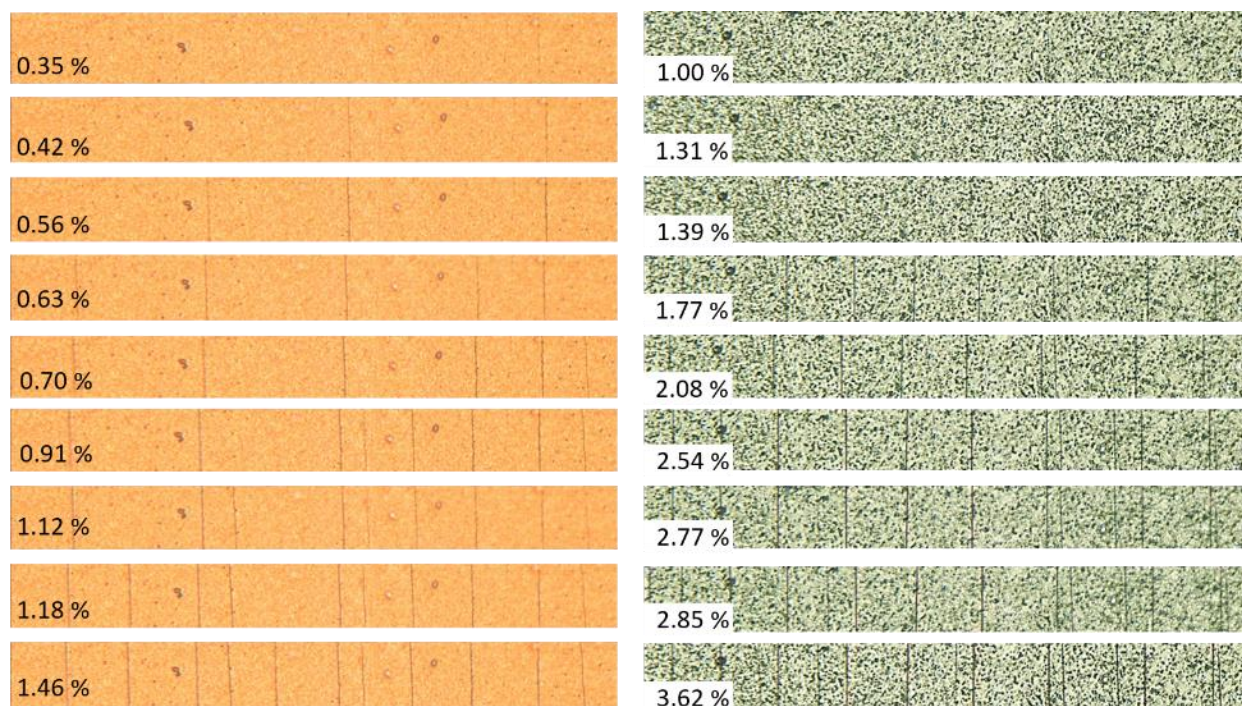


Figure 3. Micrographs of the surface of the 423 nm thick ϵ -Fe₂O₃ film (left) and of the 663 nm thick SL10 film (right) on polyimide substrate during the uniaxial tensile strain experiment. The propagation of the fragmentation process is illustrated for the strain values increasing from crack onset strain (top image) to crack density at saturation (bottom image). The cracks are seen as the dark tone vertical lines, with tensile strain acting in the horizontal direction. Width of each image is 300 μ m.

After the crack onset strain more channel cracks form with increasing strain such that the individual channel cracks are rapidly formed across the whole width of the film (Figure 3). This is characteristic behavior for brittle materials and is observed for all our thin films. The crack density along the straining axis first increases rapidly with increasing strain and then eventually saturates (Figures 3 and 4a). The fragmentation process can be modeled through Weibull statistics, such that at small strains the average fragment width L depends on strain as $L = L_0(\epsilon/\beta)^{-\alpha}$, where (L_0 is set to 1 μ m) and α and β are the Weibull shape and the scale parameters, respectively (Figure 4b).^{31, 40, 44} These parameters are useful for obtaining information on cohesive strain (ϵ_{coh}) and cohesive strength ($\sigma_{coh} = E\epsilon_{coh}$), that describe the resistance of the material to the evolution of the

fragmentation process after formation of the first crack; $\varepsilon_{coh} = \beta(1.5L_{sat}/L_0)^{-1/\alpha} \Gamma(1+1/\alpha)$, where L_{sat} is the saturation crack spacing and Γ is the gamma function.^{31, 40, 44}

The cohesive strain values are driven by the COS values, that is, they increase with increasing amount organics in the films for SL1 and SL10; the increase in the shape parameter α decreases the difference to the COS values with increasing organic content though (Table 2). For cohesive strength the increase in cohesive strain is compensated for by the simultaneous decrease in elastic modulus with increasing organic content. As a result the cohesive strength values for the ε -Fe₂O₃ and both the superlattice films are of the same order. For the Fe-TP hybrid film cohesive strength is probably lower than for the other films albeit the uncertainty in estimation of saturation crack

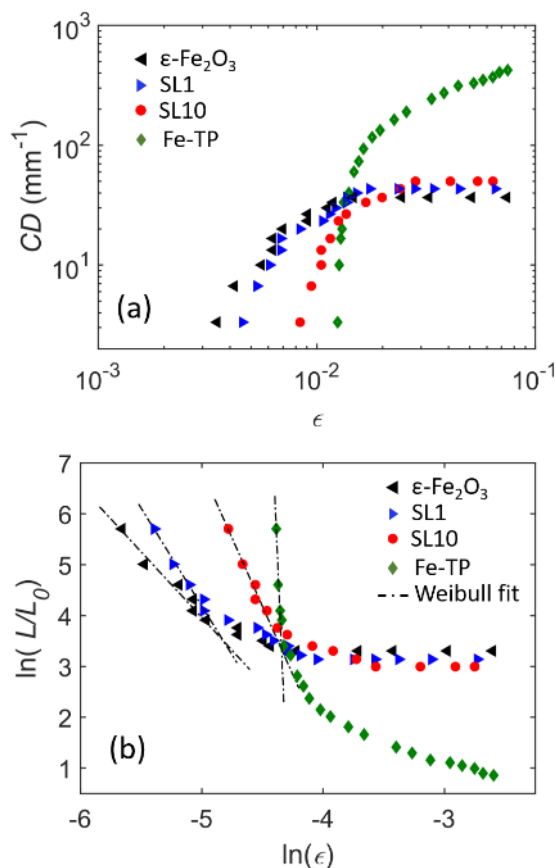


Figure 4. Fragmentation data from the uniaxial tensile tests. (a) Saturation crack density (CD) as a function of strain (ε), and (b) logarithm of normalized crack spacing (L/L_0) as a function of logarithm of strain, together with the Weibull fits.

spacing. Overall, the superlattice SL10 exhibits the best stretchability/flexibility performance of the sample series by having a high COS through inclusion of mechanically dissimilar Fe-TP layers and possibly altered residual stress, and yet reasonably high resistance to the further formation of cracks following the cracking onset owing to the cohesive properties of the inorganic layers. The broad surface features could moreover favor the high COS and cohesive properties for the SL10 (in comparison to ϵ -Fe₂O₃; see also Figure 1d), as broader features should exhibit less stress concentration at their valleys,⁴⁵ potential trigger locations for the crack formation. The Fe-TP film has equally high COS as the SL10 film, but its poor cohesion, captured nicely in the very high value of the shape parameter α , allows for very rapid evolution of the fragmentation process soon after its onset.

The onset of the fragmentation process follows inverse-square-root dependence on the film thickness ($h_f^{-1/2}$).³¹ This dependence is transferred to the cohesive strain and strength values, and hence one should be careful when comparing to literature reporting these parameters. To ease the comparison we include in Table 2 parameter values corresponding also to the thickness values of 100 nm and 50 nm, scaled through the $h_f^{-1/2}$ dependence. For example, a cohesive strength value 2454 MPa for our oxide-organic superlattice SL10, as scaled to 100 nm, is somewhat above value of 1500 MPa reported for 100-nm all-oxide SiO₂ films.³¹ On the other hand, the COS value for 100-nm SL10 of 2.3% would still be notably lower than the 9.9 % recently achieved for 100-nm alucone films grown from long and flexible organic precursors (TMA/decanediol process).³⁶ Our extrapolated COS value of 3.2 % for 50-nm SL10 is factor of three higher than for all-inorganic 50-nm Al₂O₃ and ZnO.³⁵ Overall, our oxide-organic superlattice approach thus appears to provide a route to improved flexibility/stretchability, not only in comparison to our reference oxide ϵ -Fe₂O₃, but also in comparison to oxide thin films in general.

Table 2. Fracture properties for the thin films: critical bending radius (R_c) on 50- μ m thick polyimide, crack onset strain (COS), elastic modulus (E), cohesive strain (ϵ_{coh}), and cohesive strength (σ_{coh}). The error bars represent the standard deviation over 3-5 measurements. The data for COS, R_c , ϵ_{coh} and σ_{coh} are normalized to the film thickness of 450 nm. Data extrapolated to 100 nm and 50 nm is also shown for reference for the SL10 film. For the data without normalization see Table S1.

Sample	R_c (mm)	COS (%)	E (GPa)	α	β	ϵ_{coh} (%)	σ_{coh} (MPa)
ϵ -Fe ₂ O ₃	7.7 \pm 0.3	0.33 \pm 0.01	152 \pm 33	2.8 \pm 0.4	0.027 \pm 0.008	0.56 \pm 0.08	848 \pm 120
SL1	5.3 \pm 0.2	0.48 \pm 0.02	145 \pm 37	5.0 \pm 1.1	0.015 \pm 0.004	0.66 \pm 0.06	953 \pm 80
SL10	2.4 \pm 0.3	1.07 \pm 0.13	70 \pm 20	6.8 \pm 1.7	0.021 \pm 0.003	1.48 \pm 0.09	1030 \pm 58
Fe-TP	2.6 \pm 0.2	0.99 \pm 0.08	32 \pm 8	39 \pm 16	0.015 \pm 0.002	\geq 1.1 \pm 0.09	\geq 350 \pm 27
SL10 100 nm	1.1	2.3	-	-	-	3.5	2454
SL10 50 nm	0.79	3.2	-	-	-	5.3	3662

3.4 Interface properties

The characteristics of the fragmentation patterns at higher strain values bear a connection to the film-substrate interface properties. For well-adhered films the energy required for crack formation can be transferred from the substrate to the film through a shorter film/substrate interface length (shear transfer length; along the straining axis), than for poorly-adhered films. Once the crack spacing becomes similar to the shear transfer length, the interface can no longer mediate enough energy for crack formation, and the cracking process saturates. Hence, the crack spacing at saturation (L_s) is indicative of adhesion of the film to the substrate, such that well-adhered films have shorter L_s than poorly adhered ones. Further quantification can be proceeded in terms of interfacial shear strain (or adhesive strain; ϵ_i) and interfacial shear strength ($\sigma_i = \epsilon_i E$) such that $\epsilon_i = 1.337 \epsilon_{coh} h_f / L_s$.⁴⁴

The saturation crack spacing is at least an order of magnitude smaller for the Fe-TP films than it is for the ϵ -Fe₂O₃ film (Table 3, Figures 4 and 5). For interfacial shear strain the high cohesive strain

value for the Fe-TP film drives the relative difference between ϵ -Fe₂O₃ and Fe-TP even higher, while for the interfacial shear strength the difference decreases again owing to the substantially lower elastic modulus of Fe-TP. The interfacial shear strain value of 0.01% for the ϵ -Fe₂O₃ film is close to those for other ALD-prepared oxide coatings on polyimide, in the range 0.02-0.04%.³⁵ The interfacial shear strain and strength estimates of 0.2% and 67 MPa for Fe-TP film fall in the ranges of 0.12-0.30% and 48-120 MPa observed for related alucone hybrid films.⁴⁰ The data for the ϵ -Fe₂O₃ and SL1 films do not show substantial difference, while the results for the SL10 film indicate somewhat improved adhesion in comparison to the ϵ -Fe₂O₃ film. Yet, the data for SL10 groups much closer to the data for ϵ -Fe₂O₃ than to the data for the Fe-TP film. This implies (expectedly) that the adhesion for the superlattices is dominated by ϵ -Fe₂O₃ that serves as the layer forming the interface with the substrate. Conversely though, the results suggest the Fe-TP could be used as an interface layer to improve the adhesion of the magnetically relevant ϵ -Fe₂O₃ and superlattice films.

Table 3. Interfacial properties for the film/substrate systems (polyimide substrate): saturation crack density (CD_s), saturation crack spacing (L_s), interfacial shear strain (ϵ_i), and interfacial shear strength (σ_i). The error bars represent the standard deviation over 3-5 measurements. The data is normalized to the film thickness of 450 nm. For the data without normalization see Table S2.

Sample	CD_s (mm ⁻¹)	L_s (μm)	ϵ_i (%)	σ_i (MPa)
ϵ -Fe ₂ O ₃	32±4	31±4	0.011±0.003	17±4
SL1	39±9	27±8	0.016±0.005	23±7
SL10	66±8	15±2	0.058±0.007	41±5
Fe-TP	≥317±9	≤3.2±0.09	≥0.21±0.011	≥ 67±4

Increasing tensile strain also drives increasing compressive strain into the film/substrate system in the direction perpendicular to the tensile straining axis (Poisson contraction). The compressive stress leads to the buckling (local debonding) of the film and (often) to formation of transverse cracks through fracture of the buckles at their apex. Following the onset of the buckling further

delamination of the film may gradually follow. In our case we observe formation of buckles and transverse cracks for the ϵ -Fe₂O₃ and the superlattice films but not for the Fe-TP hybrid film (Figure 5). The (tensile) buckling onset strain values for the ϵ -Fe₂O₃, SL1 and SL10 are $1.40 \pm 0.36\%$, $1.43 \pm 0.13\%$ and $2.28 \pm 0.97\%$, respectively; the SL10 thus seems to have a tendency to buckle at higher tensile strain values although the data exhibits some scatter in this respect. At tensile strain values of around 3-4% the debonding of the films is yet localized below the buckles, while increasing the strain to around 7% leads to an increase in the debonded interface area (and near complete delamination afterwards) for the ϵ -Fe₂O₃ and SL1 films. Again, the adhesion of the SL10

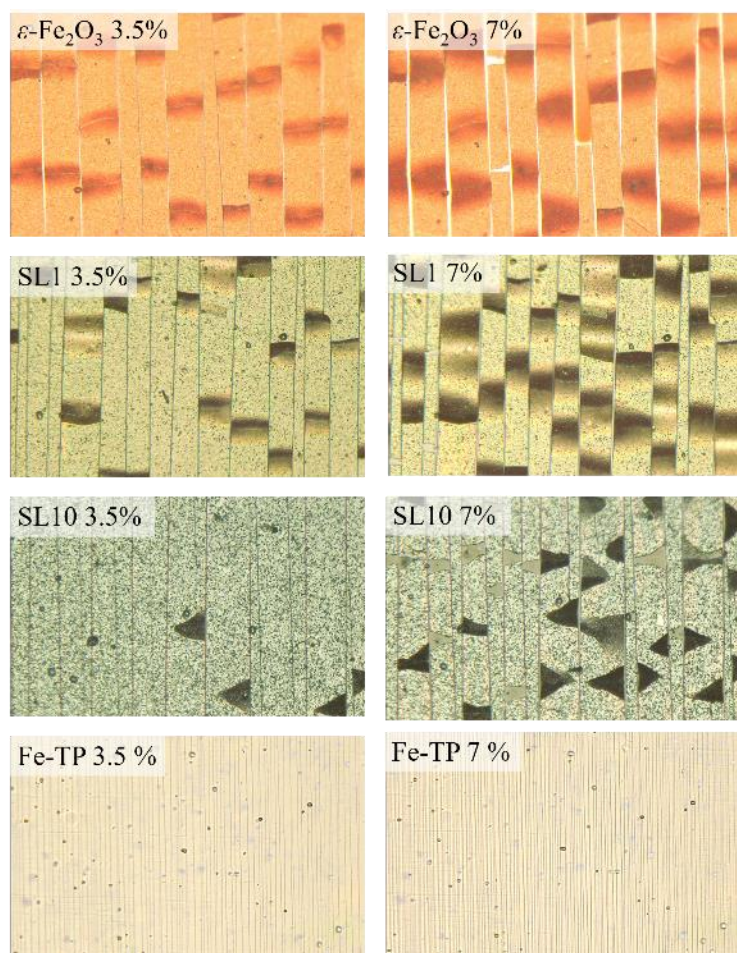


Figure 5. Representative optical micrographs for the ϵ -Fe₂O₃, SL1, SL10 and Fe-TP films under tensile strain values of 3.5% and 7%. Width of each image is 300 μ m.

1
2
3 film appears slightly better in the sense that the debonding remains more localized at higher strain
4
5 values.
6
7

8
9 Most of the buckles form "instantaneously" in view of the used imaging frequency of 1 image per
10
11 0.014% (tensile strain). However, in some cases we are able capture the onset and shape evolution
12
13 of individual buckles; see Figure S1 for example images for the ϵ -Fe₂O₃ film. Through these
14
15 observations we note that the buckling appears to onset at one edge of a fragment, evolve into a
16
17 triangular top-view shape, propagate to the other edge of a fragment and thereby obtain rectangular
18
19 shape. This observation is in contrast to the picture (proposed for metal films on polymer
20
21 substrates) in which a rectangular buckle forms from the two triangular buckles merging at the
22
23 center of a fragment.⁴⁶ Formation of a transverse crack at the apex of a buckle is often immediate
24
25 in the sense that crack forms along the course of the propagation of the buckle to the other edge of
26
27 the fragment. We observe both rectangular and triangular buckles for the ϵ -Fe₂O₃ and both the
28
29 superlattice films, such that for the ϵ -Fe₂O₃ and SL1 films the rectangular shape is more typical,
30
31 while for the SL10 film the propagation of the buckles often stops before reaching the other edge
32
33 of the fragment and the triangular shape is maintained (Figure 5). The predominance for triangular
34
35 buckles for the SL10 film could be due to its somewhat higher thickness;⁴⁷ when rectangular
36
37 buckles are formed in the SL10 film they often spall off immediately after their formation.
38
39
40
41
42
43
44
45
46

47 **3.5 Magnetic properties**

48
49

50 We characterized the magnetic properties of the unstrained ϵ -Fe₂O₃/Fe-TP films in detail in our
51
52 recent work.³⁰ Low-temperature (10 K) magnetization versus magnetic field (M-H) scans indicated
53
54 that coercive field is nearly same for the pure ϵ -Fe₂O₃, SL1 and SL10 films (~ 5 kOe). Although
55
56
57
58
59
60

the Fe-TP hybrid film exhibited paramagnetic behaviour at room temperature, the SL1 and SL10 maintain the room-temperature ferrimagnetic character of ϵ -Fe₂O₃—a key characteristic for thin-film magnets—despite the insertion of paramagnetic Fe-TP interlayers and partial suppression of crystallinity seen in Figure 1b.

Here, we briefly probed the influence of cracking and buckling to the magnetic properties of ϵ -Fe₂O₃ and SL10 thin films. In order to generate channel cracks and buckles, prior to the magnetic characterization, the films were first loaded to a tensile strain value of 3.2 % and then subsequently unloaded. At 3.2 % strain both the films exhibit substantial degree of cracking, however, the ϵ -Fe₂O₃ shows notably higher degree of buckling (Figure S3). Due to the elastic recovery of the kapton substrate (yield strain 3 %) unloading leads to the substantial relaxation of the buckles, together with partial and complete closure of the cracks for the ϵ -Fe₂O₃ and SL10, respectively (Figure S3). Magnetization versus magnetic field scans indicate that for the (strained and subsequently unloaded) ϵ -Fe₂O₃ film the absolute magnetization decreases in comparison to the unstrained state of the material, while coercivity remains essentially unchanged (Figure S4). On the contrary the SL10 film shows even a slight improvement in net magnetization and coercivity. While the potential increase in magnetic performance will make an interesting future study, the data shows that the improved mechanical characteristics for the present ϵ -Fe₂O₃/Fe-TP superlattice translate to improved preservation of the magnetic characteristics upon mechanical straining/bending.

Finally, the M-H data for the strained samples indicate that the fragmentation process does not trigger a catastrophic failure of magnetic performance, as any transport phenomena (in contrast to e.g. electronic conduction) over the cracks is not be required for magnetic recording/switching. It is important to note that the spacing of the channel cracks here is on the order of 10-30 μ m, and

typical spacing of the transverse cracks is in the range of 10-100 μm . The crystal size of e.g. the $\epsilon\text{-Fe}_2\text{O}_3$ film is in the range of 100-200 nm (Figure S2), while the superlattice period for SL1 and SL10 is around 15 nm. Therefore, loss of magnetic ordering in the vicinity of the cracks may not be especially significant in comparison to grain boundary or SL interface effects. On the other hand, delamination of the films would evidently lead to device failure. Adhesion is thus a key quality for mechanically robust flexible thin-film magnets, and in this respect the potential of the Fe-TP hybrid material for its use as an adhesion layer for the magnetically relevant $\epsilon\text{-Fe}_2\text{O}_3$ and the superlattice films is highlighted.

4. Conclusions

We demonstrated tailoring of the mechanical properties of the nanoscale $\epsilon\text{-Fe}_2\text{O}_3$ thin films through insertion of mechanically dissimilar Fe-TP interlayers and formation of superlattice structures through the combinatorial ALD/MLD route, which is interesting for magnetic recording devices in sustainable next-generation flexible electronics. It was shown through nanoindentation and tensile testing studies that with the increasing interlayer thickness (up to ca. 10 nm) the flexibility of the films increases, that is, elastic modulus decreases and crack onset strain increases. As modeled through Weibull statistics of the tensile strain fragmentation data, the increase in the crack onset strain values drives increase in cohesive strain but the inverse trend for elastic modulus limits the gains in cohesive strength. The results demonstrate that the combinatorial ALD/MLD technique provides us with a means to enhance mechanical properties of—not only inorganic-organic alloys as known from the past—but also of multilayer structures with inorganic layers thick enough to generate usable functionalities, such as the high coercive field of the $\epsilon\text{-Fe}_2\text{O}_3$ phase. Magnetic characterization conducted for strained films indicates that the improved mechanical characteristics for the present $\epsilon\text{-Fe}_2\text{O}_3/\text{Fe-TP}$ superlattices translate to improved preservation of the magnetic

characteristics upon mechanical straining. We found that under tensile strain the films fracture into (lateral) micron-scale fragments that are yet large in comparison to the layer thicknesses and grain size in the present nanoscale magnets. Therefore, for prevention of catastrophic device failure, the role of adhesion is underlined and in this context Fe-TP appears as an interesting candidate for an adhesion-layer material. We believe that similar results will be achievable also for other ALD/MLD multilayer thin films of various inorganic-organic combinations, and therefore the present data will be relevant for a number of applications requiring mechanically robust functional nanoscale thin films.

ASSOCIATED CONTENT

Supporting Information. Figure S1: Optical micrographs for the ϵ -Fe₂O₃ film showing evolution of the shape of a buckle. Figure S2: A scanning-electron-microscope cross-section view of the ϵ -Fe₂O₃ film on Si substrate. Figure S3: Optical micrographs for the ϵ -Fe₂O₃ and SL10 films after straining and subsequent unloading. Figure S4 Magnetization vs. magnetic field curves for the ϵ -Fe₂O₃ and SL10 films after straining. Tables S1 and S2: original, not normalized parameters related to the Weibull analysis.

AUTHOR INFORMATION

Corresponding Author

*janne-petteri.niemelae@empa.ch

Author Contributions

The manuscript was written through contributions of all authors. All authors have given approval to the final version of the manuscript.

ACKNOWLEDGMENT

EMPAPOSTDOCS-II programme is acknowledged; it has received funding from the European Union's Horizon 2020 research and innovation programme under the Marie Skłodowska-Curie grant agreement (754364). We also acknowledge the funding from Academy of Finland (296299), and the use of the RawMatTERS Finland Infrastructure (RAMI) and OtaNano - Nanomicroscopy Center (Aalto-NMC) at Aalto University.

REFERENCES

- (1) Ohkoshi, S.; Namai, A.; Yoshikiyo, M.; Imoto, K.; Tamazaki, K.; Matsuno, K.; Inoue, O.; Ide, T.; Masada, K.; Goto, M.; Goto, T.; Yoshida, T.; Miyazaki, T. Multimetal-Substituted Epsilon-Iron Oxide ϵ -Ga_{0.31}Ti_{0.05}Co_{0.05}Fe_{1.59}O₃ for Next-Generation Magnetic Recording Tape in the Big-Data Era. *Angew. Chem. Int. Ed.* **2016**, *55*, 11403-11406.
- (2) Miller, J. S.; Epstein, A. J. Organic and Organometallic Molecular Magnetic Materials—Designer Magnets. *Angew. Chem. Int. Ed Engl.* **1994**, *33*, 385-415.
- (3) Kao, C.; Li, B.; Lu, Y.; Yoo, J.; Epstein, A. J. Thin films of organic-based magnetic materials of vanadium and cobalt tetracyanoethylene by molecular layer deposition. *J. Mater. Chem. C* **2014**, *2*, 6171-6176.
- (4) Phan, H.; Heng, T. S.; Wang, D.; Li, X.; Zeng, W.; Ding, J.; Loh, K. P.; Shen Wee, A. T.; Wu, J. Room-Temperature Magnets Based on 1,3,5-Triazine-Linked Porous Organic Radical Frameworks. *Chem* **2019**, *5*, 1223-1234.
- (5) Cornell, R. M.; Schwertmann, U. *The Iron Oxides*, 2 ed; Wiley-VCH Verlag GmbH & Co. KGaA: Weinheim, 2003; .
- (6) Gich, M.; Fina, I.; Morelli, A.; Sánchez, F.; Alexe, M.; Gàzquez, J.; Fontcuberta, J.; Roig, A. Multiferroic Iron Oxide Thin Films at Room Temperature. *Adv. Mater.* **2014**, *26*, 4645-4652.

- (7) Gich, M.; Frontera, C.; Roig, A.; Taboada, E.; Molins, E.; Rechenberg, H. R.; Ardisson, J. D.; Macedo, W. A. A.; Ritter, C.; Hardy, V.; Sort, J.; Skumryev, V.; Nogués, J. High- and Low-Temperature Crystal and Magnetic Structures of ϵ -Fe₂O₃ and Their Correlation to Its Magnetic Properties. *Chem. Mater.* **2006**, *18*, 3889-3897.
- (8) Jin, J.; Ohkoshi, S.; Hashimoto, K. Giant Coercive Field of Nanometer- Sized Iron Oxide. *Adv. Mater.* **2004**, *16*, 48-51.
- (9) Rittenberg, D. K.; Sugiura, K.; Sakata, Y.; Mikami, S.; Epstein, A. J.; Miller, J. S. Large Coercivity and High Remanent Magnetization Organic-Based Magnets. *Adv. Mater.* **2000**, *12*, 126-130.
- (10) Popovici, M.; Gich, M.; Nižňanský, D.; Roig, A.; Savii, C.; Casas, L.; Molins, E.; Zaveta, K.; Enache, C.; Sort, J.; de Brion, S.; Chouteau, G.; Nogués, J. Optimized Synthesis of the Elusive ϵ -Fe₂O₃ Phase via Sol–Gel Chemistry. *Chem. Mater.* **2004**, *16*, 5542-5548.
- (11) Kohout, J.; Brázda, P.; Závěta, K.; Kubániová, D.; Kmječ, T.; Kubíčková, L.; Klementová, M.; Šantavá, E.; Lančok, A. The magnetic transition in ϵ -Fe₂O₃ nanoparticles: Magnetic properties and hyperfine interactions from Mössbauer spectroscopy. *J. Appl. Phys.* **2015**, *117*, 17D505.
- (12) Kulkarni, S. S.; Lokhande, C. D. Structural, optical, electrical and dielectrical properties of electrosynthesized nanocrystalline iron oxide thin films. *Mater. Chem. Phys.* **2003**, *82*, 151-156.
- (13) George, S. M. Atomic Layer Deposition: An Overview. *Chem. Rev.* **2010**, *110*, 111-131.
- (14) Miikkulainen, V.; Leskelä, M.; Ritala, M.; Puurunen, R. L. Crystallinity of inorganic films grown by atomic layer deposition: Overview and general trends. *J. Appl. Phys.* **2013**, *113*, 021301.
- (15) Knez, M.; Nielsch, K.; Niinistö, L. Synthesis and Surface Engineering of Complex Nanostructures by Atomic Layer Deposition. *Adv. Mater.* **2007**, *19*, 3425-3438.
- (16) Lee, B. H.; Ryu, M. K.; Choi, S.; Lee, K.; Im, S.; Sung, M. M. Rapid Vapor-Phase Fabrication of Organic-Inorganic Hybrid Superlattices with Monolayer Precision. *J. Am. Chem. Soc.* **2007**, *129*, 16034-16041.
- (17) Dameron, A. A.; Seghete, D.; Burton, B. B.; Davidson, S. D.; Cavanagh, A. S.; Bertrand, J. A.; George, S. M. Molecular Layer Deposition of Alucone Polymer Films Using Trimethylaluminum and Ethylene Glycol. *Chem. Mater.* **2008**, *20*, 3315-3326.
- (18) Nilsen, O.; Klepper, K. B.; Nielsen, H. Ø; Fjellvåg, H. Deposition of Organic-Inorganic Hybrid Materials by Atomic Layer Deposition. *ECS Trans.* **2008**, *16* (4), 3-14.

- (19) Meng, X. An overview of molecular layer deposition for organic and organic-inorganic hybrid materials: mechanisms, growth characteristics, and promising applications. *J. Mater. Chem. A* **2017**, *5*, 18326-18378.
- (20) Yoon, B.; Lee, B. H.; George, S. M. Highly Conductive and Transparent Hybrid Organic-Inorganic Zincone Thin Films Using Atomic and Molecular Layer Deposition. *J. Phys. Chem. C* **2012**, *116*, 24784-24791.
- (21) Niemelä, J. P.; Giri, A.; Hopkins, P. E.; Karppinen, M. Ultra-low thermal conductivity in TiO₂:C superlattices. *J. Mater. Chem. A* **2015**, *3*, 11527-11532.
- (22) Tanskanen, A.; Karppinen, M. Iron-Terephthalate Coordination Network Thin Films Through In-Situ Atomic/Molecular Layer Deposition. *Sci. Rep.* **2018**, *8*, 8976.
- (23) Tanskanen, A.; Karppinen, M. Tailoring of Optoelectronic Properties of ϵ -Fe₂O₃ Thin Films Through Insertion of Organic Interlayers. *Phys. Status Solidi RRL* **2018**, *12*, 1800390.
- (24) Niemelä, J. P.; Aghaee, M.; Kessels, W. M. M.; Creatore, M.; Verheijen, M. A. Transition in layer structure of atomic/molecular layer deposited ZnO-zincone multilayers. *J. Vac. Sci. Technol. A* **2019**, *37*, 040602.
- (25) Aghaee, M.; Niemelä, J. P.; Kessels, W. M. M.; Creatore, M. On the role of micro-porosity in affecting the environmental stability of atomic/molecular layer deposited (ZnO)_a(Zn–O–C₆H₄–O)_b films. *Dalton Trans.* **2019**, *48*, 3496-3505.
- (26) Kim, K.; Jia, X.; Fuentes-Hernandez, C.; Kippelen, B.; Graham, S.; Pierron, O. N. Optimizing Crack Onset Strain for Silicon Nitride/Fluoropolymer Nanolaminate Barrier Films. *ACS Appl. Nano Mater.* **2019**, *2*, 2525-2532.
- (27) Jen, S.; Lee, B. H.; George, S. M.; McLean, R. S.; Carcia, P. F. Critical tensile strain and water vapor transmission rate for nanolaminate films grown using Al₂O₃ atomic layer deposition and alucone molecular layer deposition. *Appl. Phys. Lett.* **2012**, *101*, 234103.
- (28) Lee, B. H.; Yoon, B.; Anderson, V. R.; George, S. M. Alucone Alloys with Tunable Properties Using Alucone Molecular Layer Deposition and Al₂O₃ Atomic Layer Deposition. *J. Phys. Chem. C* **2012**, *116*, 3250-3257.
- (29) Tanskanen, A.; Mustonen, O.; Karppinen, M. Simple ALD process for ϵ -Fe₂O₃ thin films. *APL Materials* **2017**, *5*, 056104.
- (30) Philip, A.; Niemelä, J. P.; Tewari, G.; Putz, B.; Edwards, T.; Itoh, M.; Utke, I.; Karppinen, M. Flexible ϵ -Fe₂O₃-terephthalate thin-film magnets through ALD/MLD. *ACS Appl. Mater. Interfaces* **2020**, *12*(19), 21912-21921.
- (31) Leterrier, Y.; Andersons, J.; Pitton, Y.; Månson, J. A. E. Adhesion of silicon oxide layers on poly(ethylene terephthalate). II: Effect of coating thickness on adhesive and cohesive strengths. *J. Polym. Sci. B Polym. Phys.* **1997**, *35*, 1463-1472.

(32) Bronstein, L. M.; Huang, X.; Retrum, J.; Schmucker, A.; Pink, M.; Stein, B. D.; Dragnea, B. Influence of Iron Oleate Complex Structure on Iron Oxide Nanoparticle Formation. *Chem. Mater.* **2007**, *19*, 3624-3632.

(33) Gich, M.; Gazquez, J.; Roig, A.; Crespi, A.; Fontcuberta, J.; Idrobo, J. C.; Pennycook, S. J.; Varela, M.; Skumryev, V.; Varela, M. Epitaxial stabilization of ϵ -Fe₂O₃ (001) thin films on SrTiO₃ (111). *Appl. Phys. Lett.* **2010**, *96*, 112508.

(34) Tuček, J.; Zbořil, R.; Namai, A.; Ohkoshi, S. ϵ -Fe₂O₃: An Advanced Nanomaterial Exhibiting Giant Coercive Field, Millimeter-Wave Ferromagnetic Resonance, and Magnetoelectric Coupling. *Chem. Mater.* **2010**, *22*, 6483-6505.

(35) Ruoho, M.; Niemelä, J. P.; Guerra-Nunez, C.; Tarasiuk, N.; Robertson, G.; Taylor, A. A.; Maeder, X.; Kapusta, C.; Michler, J.; Utke, I. Thin-Film Engineering of Mechanical Fragmentation Properties of Atomic-Layer-Deposited Metal Oxides. *Nanomaterials* **2020**, *10*(3), 558.

(36) Niemelä, J.; Rohbeck, N.; Michler, J.; Utke, I. Molecular layer deposited alucone thin films from long-chain organic precursors: from brittle to ductile mechanical characteristics. *Dalton Trans.* **2020**, *49*, 10832-10838.

(37) Raghavan, R.; Bechelany, M.; Parlinska, M.; Frey, D.; Mook, W. M.; Beyer, A.; Michler, J.; Utke, I. Nanocrystalline-to-amorphous transition in nanolaminates grown by low temperature atomic layer deposition and related mechanical properties. *Appl. Phys. Lett.* **2012**, *100*, 191912.

(38) Glasscock, J. A.; Barnes, P. R. F.; Plumb, I. C.; Bendavid, A.; Martin, P. J. Structural, optical and electrical properties of undoped polycrystalline hematite thin films produced using filtered arc deposition. *Thin Solid Films* **2008**, *516*, 1716-1724.

(39) Miller, D. C.; Foster, R. R.; Jen, S.; Bertrand, J. A.; Seghete, D.; Yoon, B.; Lee, Y.; George, S. M.; Dunn, M. L. Thermomechanical properties of aluminum alkoxide (alucone) films created using molecular layer deposition. *Acta Mater.* **2009**, *57*, 5083-5092.

(40) Ruoho, M.; Tarasiuk, N.; Rohbeck, N.; Kapusta, C.; Michler, J.; Utke, I. Stability of mechanical properties of molecular layer-deposited alucone. *Mater. Today Chem.* **2018**, *10*, 187-194.

(41) Ashby, M. F. *Materials Selection in Mechanical Design*, 4 ed; Elsevier Ltd.: 2011; .

(42) Abbas, N.; Qin, X.; Ali, S.; Zhu, G.; Lu, J.; Alam, F. e.; Wattoo, A. G.; Zeng, X.; Gu, K.; Tang, J. Direct deposition of extremely low interface-contact-resistant Ti₂AlC MAX-phase coating on stainless-steel by mid-frequency magnetron sputtering method. *J. Eur. Ceram. Soc.* **2020**, *40*, 3338-3342.

(43) Mishnaevsky, L. L. *Computational Mesomechanics of Composites: Numerical Analysis of the Effect of Microstructures of Composites of Strength and Damage Resistance*, 1 ed; John Wiley & Sons, Ltd: Chichester, West Sussex, England, 2007; .

(44) Leterrier, Y.; Boogh, L.; Andersons, J.; Månson, J. A. E. Adhesion of silicon oxide layers on poly(ethylene terephthalate). I: Effect of substrate properties on coating's fragmentation process. *J. Polym. Sci. B Polym. Phys.* **1997**, *35*, 1449-1461.

(45) Inglis, C. E. Stresses in a plate due to the presence of cracks and sharp corners. *Proc. Inst. Nav. Archit.* **1913**, *55*, 219-241.

(46) Toth, F.; Rammerstorfer, F. G.; Cordill, M. J.; Fischer, F. D. Detailed modelling of delamination buckling of thin films under global tension. *Acta Mater.* **2013**, *61*, 2425-2433.

(47) Cordill, M. J.; Fischer, F. D.; Rammerstorfer, F. G.; Dehm, G. Adhesion energies of Cr thin films on polyimide determined from buckling: Experiment and model. *Acta Mater.* **2010**, *58*, 5520-5531.

TABLE OF CONTENTS FIGURE

